International Journal of Thermophysics, Vol. 13, No. 1, 1992

Graphite Melting Under Laser Pulse Heating[1]

C. Ronchi,[2] R. Beukers,[2] H. Heinz,[2]
J. P. Hiernaut,[2] and R. Selfslag[2]

For a long time, the solid/liquid/vapor triple point of graphite has been a subject of debate, and despite the progress in the experimental techniques adopted, the uncertainties became even greater in recent years. In the experiments described in this paper spherical graphite specimens were heated by four tetrahedrally oriented laser beams to produce a fairly uniform temperature on the surface. A sufficiently large amount of molten graphite was produced to make it possible to identify the liquid/solid transition by a conventional thermoanalytical method. The temperature was measured by multichannel pyrometry, which enabled a detailed analysis of the perturbations and errors to be carried out. The triple point of graphite was determined to be $T_t = 4100 \pm 50$ K and $p_t = 110 \pm 10$ bar.

KEY WORDS: graphite; high-speed measurements; high temperatures; laser heating; melting; triple point.

1. INTRODUCTION

The melting behavior of graphite is not yet known with adequate accuracy: in fact, the sublimation and evaporation rates of this material are so high that conventional measurement methods are hardly applicable, and liquid graphite can be produced only by heating the sample under high hydrostatic pressures, where both heating methods and temperature measurements present serious problems. Furthermore, most of the evidence for graphite melting has been inferred by indirect arguments, and some of the published experiments have not been decisive.

[1] Paper presented at the Second Workshop on Subsecond Thermophysics, September 20–21, 1990, Torino, Italy.

[2] Commission of the European Communities, Joint Research Centre, Karlsruhe Establishment, European Institute for Transuranium Elements, 75 Karlsruhe, Germany.

0195-928X/92/0100-0107$06.50/0

In previous graphite melting experiments, heating was usually produced by direct electrical discharge or laser irradiation and the melting point was detected by analyzing the temperature evolution of the sample during the heating or cooling stages at defined energy deposition or loss rates. Despite the nominal accuracy of the various methods used, the melting temperature has so far been determined within a scatter of over 1000 K. The reasons for the experimental errors concern partly the difficulty of obtaining correct temperature measurements in the presence of large sublimation/vaporization processes, which are difficult to control, and partly the heat losses which are linked to the thermohydraulic motion of the buffer gas surrounding the sample (affecting the saturation conditions and the convective transport of the vapor) and of the molten mass itself. These effects make it difficult to interpret the thermal response of the sample to the energy input.

The results reported here have been obtained with an experimental method in which most of the uncertainty factors have been minimized, and the experimental conditions selected with the aim of producing unambiguous and directly detectable melting effects.

2. REVIEW OF PREVIOUS RESULTS

A great interest in liquid carbon was aroused, at the end of the past century, from the belief that high-pressure melting and rapid cooling of graphite could have provided a way to produce synthetic diamond. In the following decades, due to the limitations of the available experimental techniques, the studies on graphite melting were based on conjectures and models constructed from extrapolations of thermochemical and thermodynamic properties (see, e.g., Ref. 1). The earliest attempt to measure the melting point of graphite dates back to the 1930s [2]. However, it was in 1963 that Bundy [3] investigated the problem in the wider context of the high temperature–high pressure phase diagram of carbon and measured the pressure dependence of T_m up to 130 kbar by using a flash heating technique. The graphite/liquid/vapor triple point was assessed to be around 4000 K and 100 bar, and the melting temperature was found to increase slightly less than linearly with pressure, with a slope of approximately $0.0157\ \mathrm{K \cdot bar^{-1}}$. A diamond/graphite/liquid triple point was also found at 4100 K and 120 kbar. On the basis of these results, the melting line of graphite could be traced in the p–T phase diagram of carbon (Fig. 1). A few years later Schoessow [5], using a similar technique, found a graphite/liquid/vapor triple point at 4200 to 4300 K for technical grade graphite, depending on the material used, with a triple-point pressure of 100 bar. More recently, Diaconis et al. [6], using arc- and resistively heated sam-

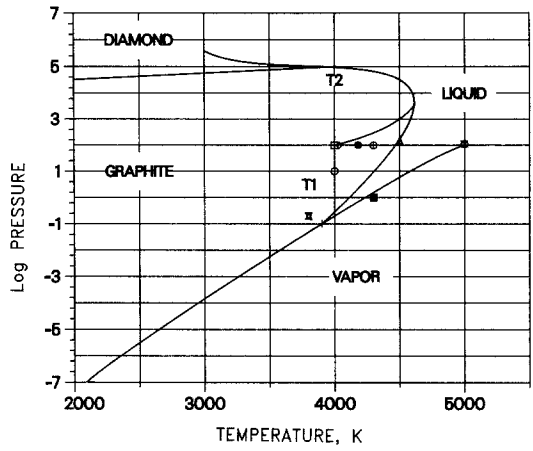

Fig. 1. The low-pressure region of the p–T phase diagram of carbon with the various experimental determinations of the graphite/liquid/vapor triple point T1 (see also Table I). Two graphite melting lines between the triple points T1 and T2 are tentatively traced. Pressure is in bars.

ples, determined the melting temperature to be in the range 4100–4300 K, at 100 bar, depending on the heating mode of the material. These results have been confirmed by Gokcen et al. [7], who reported the triple point to be at 4230 K and 110 bar for pyrolytic graphite. Vereshchagin and Fateeva [8, 9] heated graphite by passing an AC current through cylindrical pellets for several seconds. An indirect method was adopted to obtain the melting temperature, by measuring the heating power needed to melt the sample and assuming a linear dependence of C_p on temperature. T_m was found to vary from 4030 to 4100 K by increasing the pressure from 100 to 3000 bar. These investigators carried out measurements up to 80 kbar, finding a graphite melting line qualitatively similar to that produced by Bundy [10]. More recently, Venkatesan et al. [11] used pulsed laser heating to melt graphite. The molten layer formed was a few hundred nanometers thick and was revealed by Rutherford back-scattering channeling [11, 12]. The melting point was deduced by a rather complex fitting of the solution of the heat transport and dissipation equation; a value of 4300 K was obtained.

On the other hand, the graphite/liquid/vapor triple point has been determined by vapor pressure measurements in the sublimation and evaporation region over a wide pressure range. In the phase diagram in Fig. 1 the equilibrium vapor pressure curve was traced from the recommended JANAF data. The scatter of the single experimental measurements

is very large, yet it immediately appears that the triple point determined from these measurements is bound to fall very distant from most of the above mentioned measurements. In fact, Kirillin et al. [13, 14] obtained $T_t = 5000 \pm 200$ K and $p_t = 100$ bar, whereas Whittaker et al. [15] found a much lower triple point ($T_t = 3800$ K and $p = 0.12$ bar). In both cases, a laser heating technique was adopted. Kirillin et al. calculated the equilibrium pressure from the steady-state conditions attained when the heat losses due to vaporization are equal to the energy input rate. The triple-point temperature was taken to be the temperature corresponding to the triple-point pressure of 102 bar, determined from literature data. These authors pointed out that in the p–T Arrhenius diagram, the vapor–liquid equilibrium line and the sublimation line intersect, within the experimental error, at 5000 K. This is certainly a strong argument in favor of their measurement.

In the work of Whittaker et al. the triple point was deduced from the presence of a kink on the curve of the deposited laser energy versus temperature. Though the measured triple-point temperature is not very far from other measurements, some objections could be raised for this experiment, as an extremely low triple-point pressure was found (0.1 bar). In fact, experience shows that the determination of the deposited energy balance in laser pulses at these pressures is subject to very large errors due to sublimation, changes in reflectivity with temperature, and absorption–refraction effects in the vapor, which may be misleading in interpreting apparent discontinuities in the slope of the curve of energy input versus temperature.

The various results concerning melting of graphite at low pressure in the vicinity of the triple point are summarized in Table I. It can be seen that most of the results are scattered in the interval 3800–4300 K. The discrepancies are still large, but they are explained by the difficult conditions under which heating and temperature measurements are performed. In fact, the experimental errors reported in some of the works mentioned pertain to the reproducibility of the results but do not account for possible systematic errors in the treatment of the primary data.

More serious is the discrepancy of the results of Kirillin et al., in part confirmed by Cezairliyan and Miiller [16], which can hardly be attributed to differences in the accuracy of measurement.

Concerning the inconsistency of the various measurements of the triple point, a word should be said on the particular features of the graphite melting line $T_m = T_m(p)$ and the implications of the various experimental results. This line, measured by Bundy [3] and Fateeva and Vereshchagin [8], is stretched between the two triple points graphite/liquid/vapor (T1) and graphite/diamond/liquid (T2). Based on the data of these authors, the line shows a maximum around 4500–5000 K and 50–70 kbar. Since the

Table I. Low-Pressure Melting Point of Graphite

Reference(s)	T (K)	p (bar)	Technique
Basset [2]	4000	100	Flash heating
Bundy [3]	4000	—	Flash heating
Cezairliyan et al. [16]	4530	150	Resistive pulse heating
Diaconis et al. [6]	4100–4300	102	Arc heater and resistance heater
Gokcen et al. [7]	4130	120	Continuous HF laser heating
Scheindlin [14]	5000	102	Steady-state laser heating
Malvezzi et al. [4]	3900	—	Laser heating (20 ps)
Schoessow [5]	4180–4300	100	Axial centerline resistive heating
Steinbeck et al. [12]	4300	1	Laser heating of ion implanted samples
Vereshchagin et al. [9]	4035	100	Resistive heating
Whittaker et al. [15]	3800	0.1	Transient laser heating

melting entropy of graphite ΔS is expected to be positive, the Clausius–Clapeyron equation,

$$\frac{\Delta S}{\Delta V} = \frac{\partial p}{\partial T_m}$$

predicts an expansion upon melting ($\Delta V > 0$) in the low-pressure region and a contraction ($\Delta V < 0$) in the high-pressure region. Now if the graphite/liquid/vapor triple-point temperature really lies around 5000 K, then the melting line would display a different pattern, decreasing monotonically with p, i.e., it would display "anomalous" behavior, involving a densification upon melting. Interestingly, this is the case of Si and Ge, two covalent substances which have a metallic liquid phase and which have often been taken as references for scaling models of liquid graphite. The position of the triple point is therefore important for a consistent theory of liquid graphite.

3. EXPERIMENT

Spheres of fine-grain graphite were heated in an autoclave with four, tetrahedrally oriented, Nd–YAG laser beams. The material was produced by Ringsdorff-Werke with quality specification RW1. Impurities and physical properties are listed in Table II.

The spheres of 0.5- to 1-mm diameter were mechanically shaped at the top of a pin to which they were connected through a neck of 0.2-mm

Table II. Chemical and Physical Properties of Graphite RW1

Grain size (μm)	<75
Porosity (% th.d.)	13
Hardness (shore)	25
Density ($g \cdot cm^{-3}$)	1.55
Impurities (ppm)	
B	<0.01
Ca	<0.02
Cu	<0.08
Fe	<0.2
Mg	<0.1
Si	0.2
Ti	<0.5
V	<0.2

diameter and 2-mm length in order to reduce heat losses due to conduction along the mechanical support.

During laser irradiation, the surface of the sample was completely covered by the four impinging beams, whose size and power profiles were suitably adapted to obtain a fairly uniform spherical distribution of the deposited power, with spatial variations of less than 20% of the maximum value. During the cooling stage, the corresponding surface temperature differences on the area measured by the pyrometer were calculated to be less than 2% of the average. The integral energy input was fixed at 60–80 J and the pulse time was varied systematically from 0.001 to 0.1 s, corresponding to a surface power range of 10^7–10^5 $W \cdot cm^{-2}$.

Additional heating experiments have been performed with recrystallized pyrographite and highly oriented pyrographite (HOPG). These samples were in the form of thin parallelepipeds (of approximately $1 \times 1 \times 10$ mm), one extremity of which was thinned and heated under the same conditions as mentioned above. Due to the shape of the sample and to the lower thermal conductivity of HOPG along the *c*-axis, the heating was in this case nonhomogeneous and higher temperatures were produced on the surface corresponding to the hexagonal lattice plane.

The temperature of the sample was measured through a sapphire window with a six-wavelength pyrometer [17] working in the submillisecond range. The precision of this instrument is better than 0.1% in the temperature interval 3000–4000 K under the calibration conditions described in Ref. 17.

The autoclave was filled with inert gas (helium or argon) at pressures up to 1200 bar. The graphite samples were normally heated up to temperatures far above the expected melting point. During the cooling stage

following the laser switch-off, the heat losses (due to radiation, vaporization, and convection) were regular and reproducible, with a maximum achieved cooling rate of the order of $10^6\ \mathrm{K}\cdot\mathrm{s}^{-1}$. A detailed description of the thermal conditions in this type of experiment is given in Ref. 18.

The groups of six signals from the pyrometer were stored at time intervals of 0.1 ms and subsequently processed by a computer to evaluate the temperature and its confidence limits. The behavior of the sample during the laser pulse was monitored and recorded with a TV camera.

4. TEMPERATURE MEASUREMENT TECHNIQUE

Six-wavelength pyrometry is a very powerful method for the measurement of temperature when the sample emissivity is unknown and when uncontrolled optical absorptions may be present in the environment. However, the evaluation of temperature and spectral emissivities is obtained from the six pyrometer signals by assuming an ε–λ relation, which is selected on the basis of both mathematical and experimental considerations that are briefly discussed here.

From the six signals of the pyrometer V_k, $k = 1,..., 6$, a system of nonlinear equations is written of the type

$$f_k = V_k - \varepsilon_k A_k P(\lambda_k, T) = 0 \qquad k = 1,..., 6 \tag{1}$$

where $P(\lambda, T)$ is the Planck function, ε_k is the spectral emissivity at the detected wavelength λ_k, and A_k is the calibration coefficient of the kth channel. Since the number of unknowns, emissivities and temperature, exceeds by one the number of equations, Eq. (1) is solvable only if at least one additional relation between the unknowns is given. This is physically the case because the spectral emissivities are functions of the respective emitted wavelengths, and since this function is a priori undefined, its form has to be tentatively assessed in terms of a limited number of parameters M (in our case $M \leqslant 5$). Obviously, if $\varepsilon = \varepsilon(\lambda)$ is a regular function[3] and if the wavelength interval is sufficiently small, its series development can be reasonably truncated and expressed as a polynomial:

$$\varepsilon(\lambda) = \sum_{j=0}^{M-1} a_j \lambda^j \tag{2}$$

[3] In our case, we used the logarithm of the emissivity as unknown in order to restrict the physical variable to the positive field. This is a merely operative choice which accelerates the numerical computation and affects the results only within the calculated errors.

for $\lambda_{\min} \leqslant \lambda \leqslant \lambda_{\max}$. With the variable substitution of Eq. (2), Eq. (1) is transformed into a determined or overdetermined system of six equations in $M+1$ ($M \leqslant 5$) unknowns (a_k, T), which is solved numerically by a least-squares method. Intuitively, one would be inclined to assume for $\varepsilon(\lambda)$ the polynomial expression of highest permissible grade, yet the error analysis reveals that the fitting accuracy is limited by the effective experimental error. In fact, the sensitivity of the solution of Eq. (1) to the variations of the signals V_k increases with increasing M. An objective criterion for the choice of M is therefore the minimization of the local standard error of temperature, expressed as

$$\sigma_T = \sqrt{\sum_{j=1}^{6} \left(\frac{\partial T}{\partial V_j}\right)^2} \max(\sigma_{\text{exp}}, \sigma_{\text{fit}}) \tag{3}$$

where σ_{fit} is the fitting standard deviation and σ_{exp} is the real experimental error, including all expectable perturbations (signal noise, temperature heterogeneities, and possible chromatic absorptions in the ambient). It should be noted that σ_{fit} is given by

$$\sigma_{\text{fit}} = \sqrt{\sum_{k=1}^{6} \frac{f_k^2}{6-(M+1)}} \tag{4}$$

as $(6-M-1)$ is the number of independent determinations of the f_k's. In this context one can see that when M approaches 5, the residuals f_k have to decrease very rapidly to zero in order to keep σ_{fit} sufficiently small. For $M=5$ the residuals are nominally zero, if Eq. (1) admits an exact real solution. In practice, Eq. (1) can be solved only numerically and the computed f_k's are never zero. It is therefore difficult to predict the influence of the numerical accuracy of solving algorithms on the final temperature and emissivity errors. Generally, using high-order polynomials for describing $\varepsilon(\lambda)$ may lead to a deterioration of the results. In fact, $\partial T/\partial V_j$ markedly increases with increasing M and hence the effective error may dramatically grow when $\sigma_{\text{exp}} > \sigma_{\text{fit}}$. Furthermore, the numerical fitting procedure presents inherent limitations depending on the mathematical method used and on the power of the available computer since nonlinear regression analysis with more than three parameters may require a hardly practicable number of iterations.[4] Under optimum experimental conditions a signal precision of the order of 0.01% can be obtained, enabling an accurate

[4] The velocity of convergence is not the only difficulty. It should be clear that the nonlinear least-squares problem is far from being solved from the algebraic point of view, and though advanced numerical methods have been developed recently, the large residual problem is still a central one: there are no foolproof algorithms for the solution of Eqs. (1) and (2).

fitting to be attempted with high-order emissivity polynomials. Yet in the reported experiments the signal precision was approximately 0.5 to 1% and hence the best results were obtained by assuming a linear fitting ($M = 2$). Using higher-order polynomials involved clear overfitting effects, with larger errors in temperature and emissivities.

The accuracy of the temperature measurements was generally better than 1% (the highest temperature checked was 3685 K, the tungsten melting point, obtained in the same experimental conditions), however, during certain stages of the experiment other factors, described in the following sections, substantially augmented the experimental error.

5. RESULTS

One of the problematic aspects of pulsed laser heating is the heat transport from the surface into the inner regions of the sample. Very large temperature gradients arise along the heat diffusion path which complicate the evaluation of the deposited enthalpy and of the molten mass. Experiments were therefore started at low power levels and the radial temperature profiles were calculated with a computer code and compared with the experimental results. In these experiments the integral energy input was preestablished and its deposition time was conveniently chosen in order to attain at the end of the pulse a quasi-steady-state temperature on the surface of the sample. In subsequent shots the power was gradually increased until, in the temperature cooling curve as a function of time, a slope discontinuity was observed indicating a liquid–solid transition. Then, with the help of calculated radial temperature profiles, the pulse conditions were extrapolated to obtain a sufficiently long freezing temperature plateau; these were effectively defined by a compromise between a maximum achievable melted mass and a minimum total vaporization during the pulse. For instance, under 1000-bar gas pressure a power of the order of 10^5 W · cm^{-2} (i.e., a pulse length of 10 ms) was applied, by which the surface temperature attained peak values of the order of 6000 to 7000 K and the melted layer at the freezing point was approximately 0.05 to 0.1 mm thick. The equilibrium partial pressure of graphite at 7000 K is of the order of 1000 bar [13]; thus with buffer gas pressures equal to or above this value the expected vaporization rate during the shot would be tolerable. Yet the rapid natural convection flow established in the laminar gas layer around the sample produces a nonneglible vapor transport, which, for longer pulse times, deteriorates the measurement conditions as discussed in the following paragraphs.

An additional experimental difficulty was often encountered due to rapid movement of the molten mass on the surface of the sample. The

Fig. 2. RW graphite sample with droplets of frozen liquid (SEM micrograph).

scanning electron microscope (SEM) micrographs taken after the laser pulse show that, when the molten layer is thin, liquid displacement is governed by capillarity forces and liquid droplets are formed, denuding the underlying solid phase (Fig. 2). The analysis of the cooling curves of these pulses is hardly practicable because the area (0.01 mm^2) seen by the pyrometer may contain a liquid and a solid phase at significantly different temperatures and this would negatively affect the determination of the freezing plateau. Only when the molten layer was sufficiently thick could agglomeration and formation of droplets be prevented. A typical micrograph of a relatively homogeneously solidified sample is shown in Fig. 3.

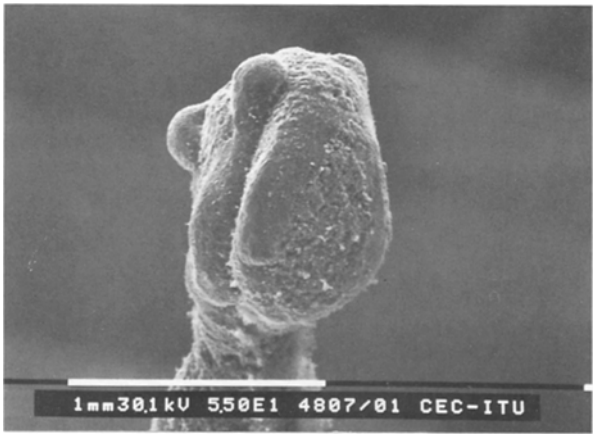

Fig. 3. RW graphite sample with frozen flowing mass of liquid (SEM micrograph).

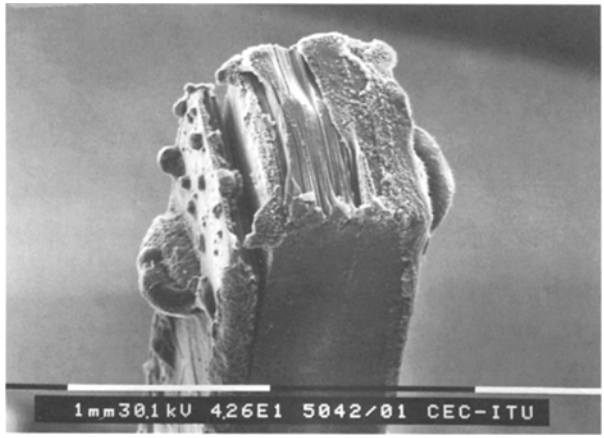

Fig. 4. HOPG sample with frozen liquid droplets on the *c*-surface (SEM micrograph).

Particularly interesting are the features produced in the recrystallized highly oriented samples (Fig. 4), where on the smooth crystallographic *c*-surface the liquid exhibits a high mobility and droplets of very different sizes are formed.

5.1. Experimental Measurements

A typical measured temperature is plotted in Fig. 5 as a function of the pulse time. It generally consists of five segments. (i) The first one

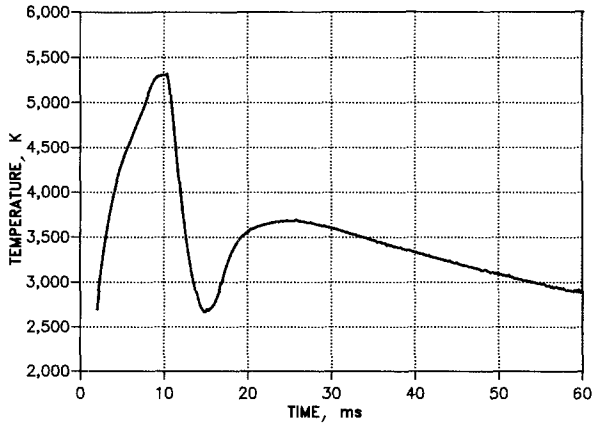

Fig. 5. Typical temperature evolution during and after a laser pulse in 50-bar helium pressure.

corresponds to the laser irradiation stage: the temperature increases rapidly until the heat losses reach the same order of magnitude as the input power. Then the heating rate decreases markedly and the temperature curve achieves a nearly constant value. (ii) At the moment when the laser is switched off, the cooling stage starts, with slopes of the order of $10^6\ \mathrm{K \cdot s^{-1}}$. The temperature decreases at approximately the same rate down to about 5000 K. During this stage the effect of the buffer gas pressure on the cooling rate is weak. (iii) Then the cooling rate decreases until the temperature reaches a minimum value $T_{\min}$, which depends on the pressure of the buffer gas: The lower the pressure, the deeper is this minimum. (iv) The temperature increases again up to a maximum, the value of which is not very reproducible at low gas pressures but, in most cases, increases with increasing pressure. (v) Finally, the sample cools regularly at a nearly constant rate, depending on the gas pressure.

5.2. Spectral Analysis of the Thermal Radiation

The measured radiance temperatures at four of the six detected wavelengths (500, 600, 700, 800, 900, and 960 nm) are plotted in Fig. 6 for a shot in helium at 500 bar. Before each experiment, the pyrometer calibration factors were checked with a laser shot on a tungsten target under the same gas pressure conditions, and its melting point at 3685 K could be measured with an error of less than 10 K. The curves in Fig. 6 clearly indicate that the measured thermal radiation of the graphite samples was highly perturbed. First, above 4500 K, the radiance temperature curve of 500 nm (and, to a lesser extent, that of 600 nm) reveals a strong depression with respect to those of the longer wavelengths. This is caused by the

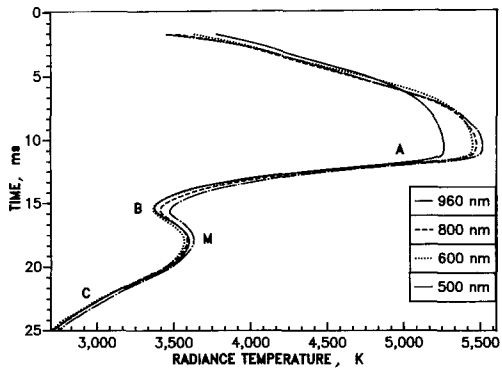

Fig. 6. Radiance temperature during a shot for four of the six detected wavelengths.

presence in the vapor of polyatomic molecules, which have high absorption bands in the visible range. In our case the main absorption is likely due to the C_2 Swann band, which is centered around 500 nm and has the largest cross section (10^{-18}–10^{-17} cm^2) [19]. With the elapse of time the 500-nm signal recovers its normal level, indicating that the absorbing vapor molecules disappear, as they rapidly cool and precipitate into soot particles. Thus, the 500-nm radiance temperature provides a useful indicator for the point where vapor molecules are formed and where they start condensing to form soot (point A in Fig. 6). The consequent absorption of thermal radiation by the soot is effectively detected by the multichannel pyrometer as a decrease in emissivity. If one considers that the radiance temperature T_R is related to the true temperature T by the equation,

$$\frac{1}{T}-\frac{1}{T_R}=\frac{\lambda \ln \varepsilon(\lambda, T)}{c_2} \tag{5}$$

where c_2 is the second radiation constant, a decrease in the emissivity results in a broadening of the radiance temperature interval. This is actually observed during the cooling stage from point A to point B. In the final stage (points B, M, and C in Fig. 6), the radiance temperature interval becomes narrower, indicating an increase in the effective emissivity, i.e., a diminution of the soot absorption.

This effect is illustrated in terms of apparent emissivity in the example in Fig. 7, where the results of a laser shot at 4700 K (i.e., just above the

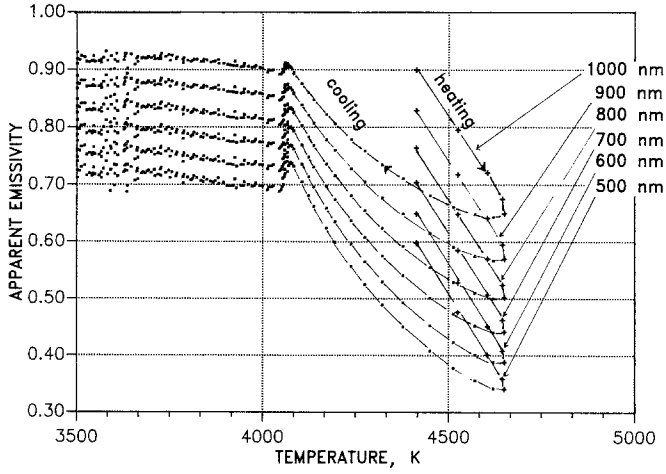

Fig. 7. Apparent emissivity of RW graphite as a function of temperature, calculated from the multichannel pyrometer signals.

temperature at which one expects substantial soot formation) are plotted. During heating the apparent emissivities are higher than during cooling, where soot is formed. The apparent emissivities increase with decreasing temperature as the soot is rapidly swept out by gas convection. Below a well-defined temperature (in this case 4100 K), the emissivity is higher and remains nearly constant.

5.3. Temperature Evaluation in the Various Stages

Though multichannel pyrometry can be used to a certain extent even in the presence of strong absorptions, the complexity of the phenomena involved requires great caution in the analysis. In order to improve, as far as possible, the accuracy of the temperature measurements over the whole field, we followed a hybrid method. The integral six-wavelength analysis was used during stages where selective color absorption was negligible. The criterion was given by the quality of the local fitting. In regions where the fitting error was too large, one or more of the shorter wavelengths were excluded.

Figure 8 shows temperature errors resulting from the integral analysis of the six signals of the pyrometer. First, one can see that the uncertainty is very large around the peak value and increases with temperature. The error remains large even during the stage where the absorption of the 500- and 600-nm radiation is absent, and vaporized carbon is present in the

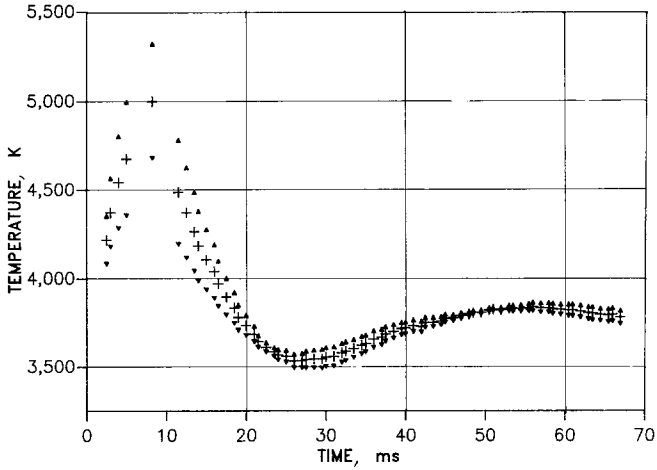

Fig. 8. Temperature errors obtained by fitting the six pyrometer signals. The average values (crosses) are indicated with the extremities of the error bars.

form of soot particles. These particles are present at very high densities in the hot gas plume, absorbing a large amount of the radiation emitted by the sample (the thickness of the gas convection layer was visualized with a light refraction method; at 1000 bar it was of the order of 0.1 mm, whereas at 100 bar it was a few millimeters). The temperature of the soot and its surface covering ratio are therefore sufficiently high to affect significantly the radiation spectrum of graphite, producing systematic errors in the temperature evaluation. With decreasing temperature, the soot density increases to such an extent that the pyrometer sees almost only the radiation emitted by these particles. The maximum soot screening effect corresponds to the observed temperature minimum. As natural gas convection removes the suspended particles, some of which are redeposited on the surface of the sample, the apparent temperature increases again until a maximum is reached, corresponding to the "clearing" point, where the gas plume becomes completely transparent. At this point the error is small, indicating that the radiating source now has a fairly homogeneous temperature. Electron micrographs of the samples after the laser shots indeed reveal the presence of soot particles on their surfaces.

The radiation absorption effect, which determines the shape of the cooling curves is, of course, proportional to the amount of evaporated material. Therefore, one expects that when the carbon vapor pressure at the peak temperature is lower than the buffer gas pressure, the absorption is less effective; in the other cases, the lower the buffer gas pressure is, the lower the measured temperature minimum T_{min} is. Actually, heating experiments, carried out at different pressures, confirm this interpretation (Fig. 9). It can be seen that above 600 bar the minimum is very weak and

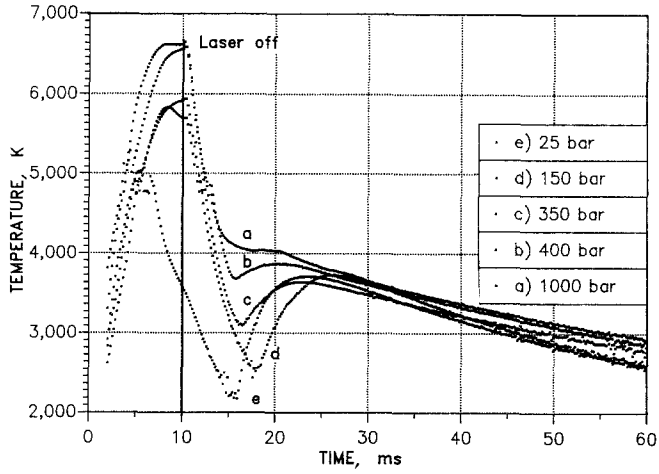

Fig. 9. Temperature evolution in pulses at various pressures.

at 1000 bar it is effectively absent. At this pressure the cooling curve consists of three segments with distinct slopes. The high-temperature segment does not differ very much from those measured at lower pressures, but at a well-defined temperature (4100 ± 50 K) a knee point is observed, followed by a horizontal plateau of a few milliseconds' duration; afterward, the temperature decrease assumes a final slope, which, in agreement with the termal convection rule, is somewhat steeper than that at lower pressures. The evaluated temperature uncertainty on the plateau is a minimum, indicating the existence of an effectively homogeneous temperature on the sample surface. The interpretation of this plateau as the liquid/solid transition is clear, as the cooling curve at 1000 bar is quite similar to those measured in a large number of other compounds where the plateau temperature was equal, within the experimental error, to the melting temperature [20].

The hypothesis that the plateau is due to a phase transition in the graphite and not to condensation of vapor or redeposition of soot particles is also confirmed by the measurement of the mass losses due to vaporization (Fig. 10). It can be seen that at 1000 bar these losses correspond to less than 5% of the initial volume of the sample and are, to a large extent, removed by the gas plume. Scanning electron microscope analysis of the sample surface after the shot reveals only sparse redeposition of particles. At lower gas pressures, the sample is increasingly covered by soot. However, down to 150 bar, large frozen melted zones emerge from the deposited soot bed; if these zones are occasionally located in the pyrometer window, a freezing plateau at 4100 K may still be detected (Fig. 11).

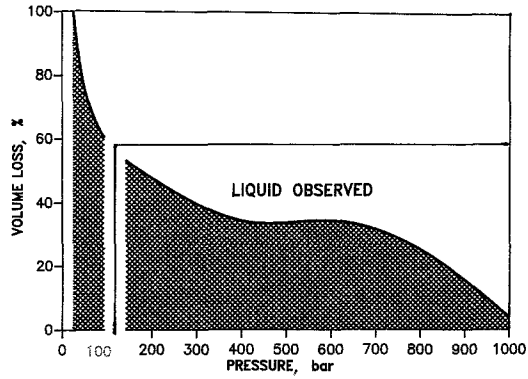

Fig. 10. Fractional graphite mass evaporated or sublimated from the sample at constant energy input as a function of gas pressure. The observed existence range of the liquid phase is indicated.

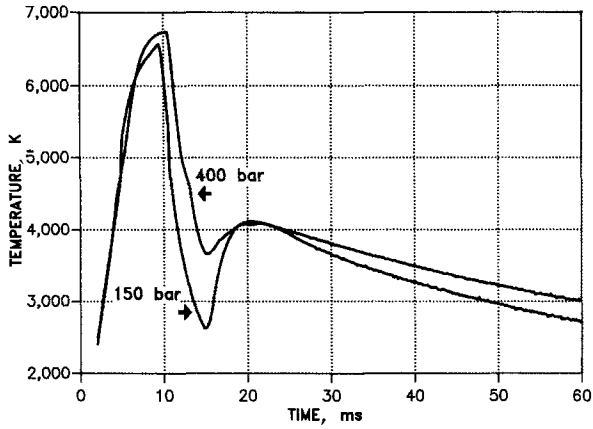

Fig. 11. Temperature evolution in two pulses at relatively low pressures where melted graphite was not covered by soot. The maximum temperature after gas clearing corresponds to the freezing plateau.

After shots with pressures below 150 bar, the specimens are almost completely covered by soot but traces of melted graphite were found at pressures as low as 100 bar (Fig. 10). One can therefore conclude that the melting temperature changes very little between 150 and 1200 bar and hence the triple point of graphite/liquid/vapor is 4100 ± 50 K and 110 ± 10 bar.

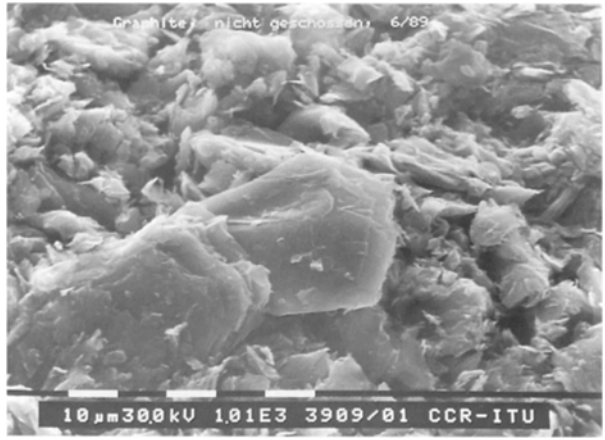

Fig. 12. Initial structure of RW graphite (SEM micrograph).

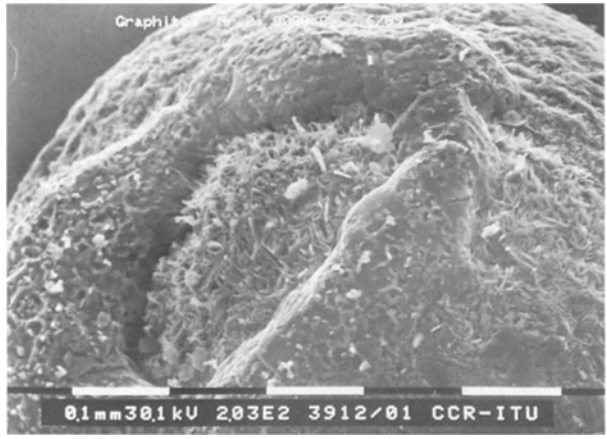

Fig. 13. Frozen molten graphite with unmelted region (SEM micrograph).

5.4. Structure Analysis

The heated graphite undergoes dramatic changes with respect to the initial structure (shown in Fig. 12). The specimens treated under high pressures (800 to 1200 bar) exhibit a brilliant surface after the shot. Macroscopically the surface is rather irregular, indicating streams of molten mass (Fig. 13) covered by a smooth crust. These are most likely produced by displacement and agglomeration of the liquid. Tracts of unmelted surface appear like islands among this mass. A microscopic observation reveals

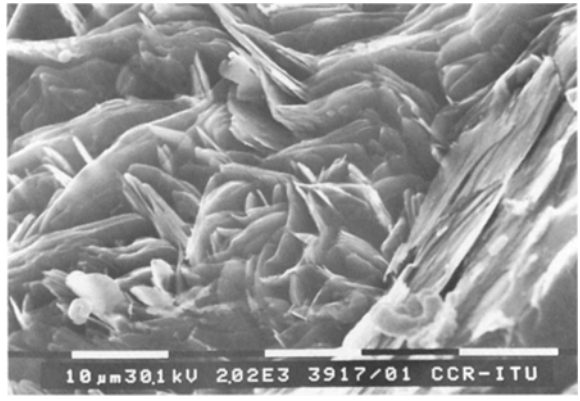

Fig. 14. Lamellar structure of the frozen liquid (SEM micrograph).

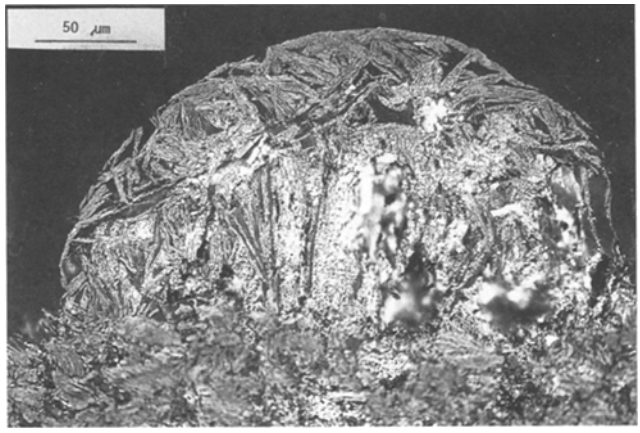

Fig. 15. Structure beneath the crust of a frozen liquid droplet (metallographic cross section).

that these zones consist of large platelets oriented parallel to the sample sphere radius, i.e., to the thermal gradient. Their patterns, seen end on, appear as an irregular honeycomb (Fig. 14). Apparently, this structure seems quite different from that of the frozen mass, however, sectional analysis shows that beneath the compact crust the same lamellar structure is present and the crust itself is formed by variably oriented platelets, producing altogether a continuous curvature (Figs. 15 and 16).

The aspect of the samples heated at lower pressures is different. Despite larger ablations, the surface is dark, with a tendency to crumble

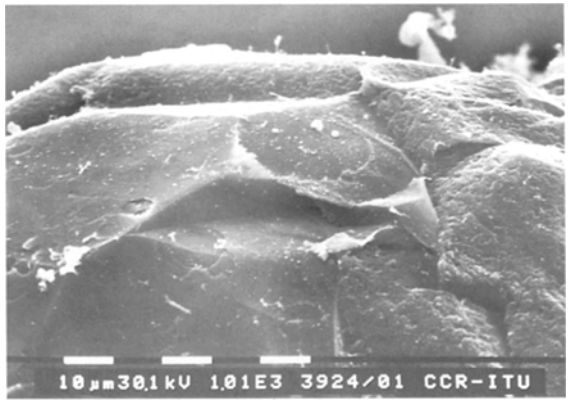

Fig. 16. Crust of a frozen liquid droplet.

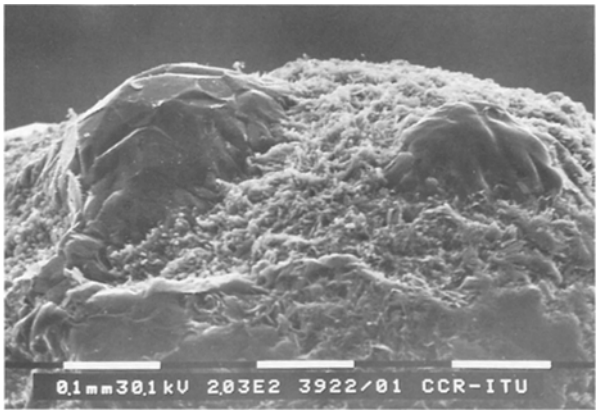

Fig. 17. Solidified zones emerging from a deposited soot bed in a sample heated under 200-bar gas pressure (SEM micrograph).

into powder. Scanning electron micrographs show that the specimens are nearly completely covered by a mass of spheroidal soot particles of a few microns size, above which rare shining zones appear elevated above the deposited soot bed (Fig. 17). These zones have the same structure as those formed from frozen liquid after pulses at high pressure and can be observed with certainty down to pressures of 110 bar. Below 100 bar they are absent.

Transmission electron microscopy of the platelets formed from solidified liquid indicates that they are single crystals with linear dimensions of several tens of microns, stacked in a lamellar structure over the hexagonal lattice plane.

5.5. Estimation of the Liquid Density

The structure of the small frozen liquid droplets permits us to draw some conclusions concerning the density of liquid graphite. In fact, the crust of the droplets, typically represented by the example in Fig. 16, is regularly shaped and unbroken. We can therefore infer that the underlying 100% dense liquid mass did not affect the outer shell of the droplet by freezing, and hence the fractional density of the frozen structure should approximately correspond to the ratio between the liquid and the solid density. Several droplets have been prepared for quantitative metallographic analysis and scanned with an image analyzer. The results were consistent for both the RW and the HOPG samples, giving a void fraction of 0.4 ± 0.05; that implies that the expansion upon melting is of the order of 70% of the solid specific volume. This is in agreement with the graphite

melting observations made by Shaner [21], who reported an increase in the specific volume of up to 100%.

This large melting expansion is in qualitative agreement with the slope of the low-pressure branch of the melting line, drawn in Fig. 1. The open structure of liquid graphite in this pressure range can hardly be consistent with a metallic model, e.g., like that of germanium, with four conduction electrons per atom. A closer analogy may be found with liquid tellurium, which has a chainlike structure with an atomic coordination number of two [the melting line $T_m(p)$ of tellurium also passes through a maximum]. Starting from this observation, Ferraz and March [22] proposed a model by which, at low pressure, an "sp"-hybridized chainlike nonmetallic liquid is formed. A liquid metal with higher atomic correlation would be stable at higher pressures (>3–5 kbar), and only above the maximum of the melting line ($T > 4500$–5000 K, $p > 50$–80 kbar) is the tetravalent metallic carbon to be expected. Based on phenomenological considerations, this model, though merely conjectural, provides a consistent explanation of the experimental results obtained so far.

6. CONCLUSIONS

A few considerations can be presented concerning the features of our graphite pulse heating experiments and their interpretation.

- Both the heating and the cooling rates of graphite during laser pulses of a few milliseconds up to above the melting point are governed mainly by vaporization processes and the radiance temperature of the sample is strongly affected by the subsequent behavior of the carbon vapor.
- At lower gas pressures the vapor is dispersed in a larger gas layer and condenses in the form of soot particles of a few microns' size, most of which are gradually redeposited on the surface of the sample, giving rise to an apparent "undercooling" of the sample.
- After complete redeposition or sweeping-out of the suspended soot, the measured temperature evolution assumes the normal trend, with a cooling rate depending on natural convection and increasing with increasing gas pressure.
- At sufficiently high pressure the carbon vapor in the surrounding buffer gas is confined within a thin laminar layer which is rapidly removed by natural convection. Little soot deposition is observed on the sample surface.

- In pulses above 1000 bar, the inflection point on the temperature-vs-time curve and the subsequent plateau at 4100 K have to be ascribed to a phase transition in the graphite. A transition at the same temperature is also observed in the spectral emissivities: below 4100 K the measured emissivities coincide with those of solid graphite; above this temperature their trend is completely different.
- No other singularities are observed in the cooling curves above 4100 K.
- Clear evidence for liquid formation is provided by metallographic examination of the heated samples at pressures above 110 bar. There are indications that the expansion upon melting is of the order of 70%.

From these observations one can conclude that the observed plateau is produced by the liquid/solid transition and the graphite/liquid/vapor triple point of graphite is $T_t = 410 \pm 50$ K and $p_t = 110 \pm 10$ bar. This result is essentially in agreement with the melting-line pattern first proposed by Bundy, however, in the p–T phase diagram a substantial discrepancy persists between the position of the triple point T1 and the measured equilibrium vapor pressure curve at high temperature.

ACKNOWLEDGMENTS

We would like to express our thanks to M. Scheindlin (IVTAN, Moscow) for stimulating discussions and for providing specimens for additional experiments in which he personally participated. We regret that our joint effort could not remove the discrepancies between the results published in this paper and those obtained by his group. Finally, we are very grateful to I. Ray, C. Sari, and H. Thiele for their valuable help in the microscopic and metallographic analyses.

REFERENCES

1. O. I. Leipunskii, *Usp. Khim.* **8**:1919 (1939).
2. M. J. Basset, *J. Phys. Radium* **10**:217 (1939).
3. F. P. Bundy, *J. Chem. Phys.* **38**:618 (1963).
4. A. M. Malvezzi, N. Bloembergen, and C. Y. Huang, *Phys. Rev. Lett.* **57**:146 (1986).
5. G. J. Schoessow, *Phys. Rev. Lett.* **21**:738 (1968).
6. N. S. Diaconis, E. R. Stover, J. Hook, and G. J. Catalano, U.S. Report, General Electric AD 727 064; AFML TR 71 119 (1971).
7. N. A. Gokcen, E. T. Chang, T. M. Poston, and D. J. Spencer, *High Temp. Sci.* **8**:81 (1976).
8. N. S. Fateeva and L. F. Vereshchagin, *Zh. Eksp. Teor. Fiz. Pis'ma Red.* **13**:157 (1971).

9. L. V. Vereshchagin and N. S. Fateeva, *High Temp. High Press.* **9**:619 (1977).
10. F. P. Bundy, *J. Geophys. Res.* **85**:6930 (1980).
11. T. Venkatesan, D. C. Jacobson, J. M. Gibson, B. S. Elman, G. Braunstein, M. S. Dresselhaus, and G. Dresselhaus, *Phys. Rev. Lett.* **53**:360 (1984).
12. J. Steinbeck, G. Braunstein, M. S. Dresselhaus, T. Venkatesan, and D. C. Jacobson, *J. Appl. Phys.* **58**:4374 (1985).
13. A. V. Kirillin, M. D. Kovalenko, M. A. Scheindlin, and V. S. Zhivopistsev, *Tepl. Vys. Temp.* **23**:699 (1985).
14. M. A. Scheindlin, *Tepl. Vys. Temp.* **19**:630 (1981).
15. A. G. Whittaker, P. L. Kintner, L. S. Nelson, and N. R. Richardson, U.S. Report, Aerospace Corp. A DA 106134/0 (1981).
16. A. Cezairliyan and A. P. Miiller, *Int. J. Thermophys.* **11**:643 (1990).
17. J. P. Hiernaut, R. Beukers, W. Heinz, R. Selfslag, M. Hoch, and R. Ohse, *High Temp. High Press.* **18**:617 (1986).
18. J. P. Hiernaut and C. Ronchi, *High Temp. High Press.* **21**:119 (1989).
19. K. Sutton and J. N. Moss, 17th Aerospace Sciences Meeting, Paper 79-0033, New Orleans, La, Jan. 15–17 (1979).
20. J. P. Hiernaut, F. Sakuma, and C. Ronchi, *High Temp. High Press.* **21**:139 (1989).
21. J. W. Shaner, *Bull. Am. Phys. Soc.* **32**:607 (1987).
22. A. Ferraz and N. H. March, *Phys. Chem. Liq.* **8**:289 (1979).